PERGAMON

International Journal of Solids and Structures 39 (2002) 1863–1883

INTERNATIONAL JOURNAL OF SOLIDS and STRUCTURES

www.elsevier.com/locate/ijsolstr

Spatially complex localisation in twisted elastic rods constrained to a cylinder

G.H.M. van der Heijden [a,*], A.R. Champneys [b], J.M.T. Thompson [a]

[a] *Centre for Nonlinear Dynamics, University College London, Gower Street, London WC1E 6BT, UK*
[b] *Department of Engineering Mathematics, University of Bristol, University Walk, Bristol BS8 1TR, UK*

Received 7 March 2001

Abstract

We consider the problem of a long thin weightless rod constrained to lie on a cylinder while being held by end tension and twisting moment. Applications of this problem are found, for instance, in the buckling of drill strings inside a cylindrical hole. In a previous paper the general geometrically exact formulation was given and the case of a rod of isotropic cross-section analysed in detail. It was shown that in that case the static equilibrium equations are completely integrable and can be reduced to those of a one-degree-of-freedom oscillator whose non-trivial fixed points correspond to helical solutions of the rod. A critical load was found where the rod coils up into a helix.

Here the anisotropic case is studied. It is shown that the equations are no longer integrable and give rise to spatial chaos with infinitely many multi-loop localised solutions. Helices become slightly modulated. We study the bifurcations of the simplest single-loop solution and a representative multi-loop as the aspect ratio of the rod's cross-section is varied. It is shown how the anisotropy unfolds the 'coiling bifurcation'. The resulting post-buckling behaviour is of the softening–hardening–softening type typically seen in the cellular buckling of long structures, and can be interpreted in terms of a so-called Maxwell effective failure load.

Keywords: Elastic rod; Anisotropy; Cylindrical constraint; Localised solutions; Multi-pulse homoclinic orbits; Softening–hardening–softening response; Maxwell failure load; Helical collapse; Drill string

1. Introduction

In a previous paper (van der Heijden, 2001) one of us used the Cosserat director theory to formulate an ordinary differential equation (ODE) model for the statics of an end-loaded rod whose centreline is constrained to lie on a rigid cylinder, but which is otherwise free to bend and twist. This problem is relevant to the petroleum and other drilling industries when dealing with buckled drill strings confined in a cylindrical hole (see, e.g., Huang and Pattillo, 2000). Applications may also be found in certain fittings in overhead transmission lines in which wires or rods are wound around a cylindrical conductor

* Corresponding author. Tel.: +44-20-7679-2727; fax: +44-20-7380-0986.
E-mail address: g.heijden@ucl.ac.uk (G.H.M. van der Heijden).

0020-7683/02/$ - see front matter
PII: S0020-7683(01)00234-7

(Seemann, 1996). Further references to these and other applications may be found in van der Heijden (2001). Although the formulation in van der Heijden (2001) applied to perfect (i.e., intrinsically straight and prismatic), inextensible and unshearable rods of arbitrary cross-section, only the case of an isotropic rod was studied, i.e., a rod with equal bending stiffnesses about its two principal axes of inertia. In that case the static equilibrium equations can be reduced to those of a one-degree-of-freedom equivalent oscillator (much like in the case of a free, i.e., unconstrained, rod studied in van der Heijden and Thompson (2000)), with arclength along the rod's axis playing the role of time. Thus, many properties of the solutions can be obtained explicitly. In particular it follows that twist is conserved along the length of the rod. Special attention was given to localised solutions which decay exponentially towards both ends of the rod and are described by homoclinic orbits of the oscillator. Heteroclinic bifurcations occur at certain values of the applied load and correspond to critical points of collapse of the straight rod into a helical coil.

It is known for the case of an unconstrained rod that non-symmetric properties of the cross-section lead to spatial chaos (see, e.g., Mielke and Holmes, 1988; van der Heijden et al., 1999a). For our purposes this manifests itself in the existence of infinitely many multi-loop localised solutions. Moreover, and similar to the case of an unconstrained rod in three dimensions (van der Heijden and Thompson, 1998; van der Heijden et al., 1999a), as well as that of a rod with planar constraint (van der Heijden et al., 1999b), anisotropy breaks the circular symmetry of the problem causing the primary single-loop localised solutions for the isotropic rod to split into two physically distinct solutions. The multiplicity of the surviving solutions may be characterised by using the reversing symmetries of the ODEs.

In the present paper we show that similar complex spatial behaviour occurs in constrained anisotropic rods. However, the bifurcation behaviour of the localised solutions is far richer here than in the free-rod case. There are fundamental differences, too. Firstly, the linear buckling load is infinite. Secondly, as the dimensionless load parameter, measuring the ratio of the square of the end moment and the tension, is reduced, it is found that there is a minimum possible value for the existence of primary, single-loop, buckling solutions. This end value is reached in a non-monotonic fashion with the load oscillating between two values. In the limit where the anisotropy vanishes, these two values can be shown to approach that of the single critical load of the isotropic problem. Thus the post-buckling response is seen to be of softening–hardening–softening type known from cellular buckling in long structures. This gives rise, in a particularly simple and understandable way, to a variant of the Maxwell load (ML) phenomenon that has recently been discovered by Hunt and his co-workers (Hunt et al., 1999, 2000; Peletier, 2001).

In more detail, the organisation of this paper is as follows. Section 2 briefly reviews the formulation of the problem of an end-loaded elastic rod constrained to lie in permanent contact with a cylinder. The constraint is enforced by introducing a distributed normal external reaction force (which may take either sign) exerted by the cylinder on the rod. By employing a cylindrical co-ordinate system the equilibrium equations are then reduced to a coupled system of six ODEs. This system is made dimensionless and its (reversing) symmetries and conserved quantities are identified. The results of van der Heijden (2001) on the isotropic case, which is completely integrable, are then briefly reviewed.

Section 3, the main section of the paper, goes on to study the anisotropic rod. It is shown numerically that complete integrability is broken (twist along the rod no longer being conserved). Single- and multi-loop solutions are computed with the aid of a shooting method which exploits the reversing symmetry of the problem. The behaviour of these localised solutions is studied as the anisotropy is varied, and a coherent picture of the effect of anisotropy is presented. Section 4 introduces the ML and shows that it can be used to generalise the critical coiling load of the isotropic case to the anisotropic case. It also seems to suggest that near-helical coiled solutions could be stable under appropriately defined end-loading conditions. Finally, Section 5 draws conclusions and comments on the physical relevance of our results.

2. The formulation of a constrained rod

Consider a weightless elastic rod lying on a cylinder and held by end tension T and twisting moment M applied in the direction of the axis of the cylinder. The forces and moments at both ends need not be co-axial and we shall assume that the loading device leaves the ends of the rod free to slide (without friction) around the circumference of the cylinder. The rod is taken to be initially straight and allowed to twist and bend. Shear deformation and axial extension will be ignored.

The Cosserat theory models such a rod as a line in space (the centreline or line of centroids of the rod) endowed with mechanical properties which are assumed to be suitable averages over the cross-section of the rod. Thus, after choosing an origin for the arclength co-ordinate s, the full configuration of the rod is defined by a right-handed rod-centred co-ordinate frame of directors $\{\boldsymbol{d}_1, \boldsymbol{d}_2, \boldsymbol{d}_3\}$ specified at each value of s. The vector $\boldsymbol{d}_3$ is taken to be tangent to the rod, i.e., $\boldsymbol{d}_3 = \dot{\boldsymbol{r}}$, where the vector function $\boldsymbol{r}(s)$ describes the centreline of the rod relative to some fixed co-ordinate system to be specified later, and the overdot denotes differentiation with respect to arclength s. (Note that $\dot{\boldsymbol{r}}$ is a unit vector in any configuration of the rod because of the inextensibility assumption.) The directors $\boldsymbol{d}_1$ and $\boldsymbol{d}_2$ are chosen along the principal axes of the second moment of area in the normal cross-section of the rod.

2.1. The equilibrium equations

If we denote the internal forces and moments along the rod by $\boldsymbol{n}$ and $\boldsymbol{m}$, respectively, then the equilibrium equations of the constrained rod are given by (see, e.g., Antman, 1995):

$$\begin{array}{ll} \dot{\boldsymbol{n}} = \boldsymbol{f} & \text{(force balance)}, \\ \dot{\boldsymbol{m}} + \dot{\boldsymbol{r}} \times \boldsymbol{n} = \boldsymbol{0} & \text{(moment balance)}, \\ \dot{\boldsymbol{r}} = \boldsymbol{d}_3 & \text{(centreline equation)}, \\ \dot{\boldsymbol{d}}_i = \boldsymbol{u} \times \boldsymbol{d}_i, \quad i = 1,2,3 & \text{(director frame equations)}. \end{array} \tag{1}$$

Here an initially unknown external body force per unit arclength $\boldsymbol{f}$ (but no such moment) is assumed to act normal to the cylinder. $\boldsymbol{u} = u_1 \boldsymbol{d}_1 + u_2 \boldsymbol{d}_2 + u_3 \boldsymbol{d}_3$ is the generalised strain vector whose components with respect to the director basis are the curvatures and the twist. We will take linear constitutive relations between the generalised stresses and strains:

$$u_1 = \frac{1}{B_1} \boldsymbol{m} \cdot \boldsymbol{d}_1, \quad u_2 = \frac{1}{B_2} \boldsymbol{m} \cdot \boldsymbol{d}_2, \quad u_3 = \frac{1}{C} \boldsymbol{m} \cdot \boldsymbol{d}_3, \tag{2}$$

where B_1 and B_2 are the bending stiffnesses about $\boldsymbol{d}_1$ and $\boldsymbol{d}_2$, respectively, and C is the torsional stiffness.

Let $\{\boldsymbol{e}_1, \boldsymbol{e}_2, \boldsymbol{e}_3\}$ be a fixed right-handed orthonormal co-ordinate system. Because of the geometry of the problem it is convenient to introduce cylindrical co-ordinates (r, ψ, z) for the position vector,

$$\boldsymbol{r} = r\cos\psi\, \boldsymbol{e}_1 + r\sin\psi\, \boldsymbol{e}_2 + z\, \boldsymbol{e}_3, \tag{3}$$

and to define a cylindrical co-ordinate frame $\{\boldsymbol{e}_r, \boldsymbol{e}_\psi, \boldsymbol{e}_z\}$ with $\boldsymbol{e}_r$ taken normal to the cylinder, $\boldsymbol{e}_\psi$ in the circumferential direction, and $\boldsymbol{e}_z$ in the direction of the axis of the cylinder and the applied wrenches:

$$\begin{aligned} \boldsymbol{e}_r &= \cos\psi\, \boldsymbol{e}_1 + \sin\psi\, \boldsymbol{e}_2, \\ \boldsymbol{e}_\psi &= -\sin\psi\, \boldsymbol{e}_1 + \cos\psi\, \boldsymbol{e}_2, \\ \boldsymbol{e}_z &= \boldsymbol{e}_3. \end{aligned} \tag{4}$$

Vectors are expressed with respect to the cylindrical co-ordinate frame using the following notation: $\boldsymbol{n} = n_r \boldsymbol{e}_r + n_\psi \boldsymbol{e}_\psi + n_z \boldsymbol{e}_z$, $\boldsymbol{m} = m_r \boldsymbol{e}_r + m_\psi \boldsymbol{e}_\psi + m_z \boldsymbol{e}_z$, $\boldsymbol{d}_i = d_{ir} \boldsymbol{e}_r + d_{i\psi} \boldsymbol{e}_\psi + d_{iz} \boldsymbol{e}_z$ $(i = 1,2,3)$. The equilibrium equations (1) can now be expressed in cylindrical co-ordinates by using Eq. (4). For instance, for the components of $\boldsymbol{d}_3$ we have

$$\begin{aligned}\dot{d}_{3r} &= d_{3\psi}^2/r + u_2 d_{1r} - u_1 d_{2r},\\ \dot{d}_{3\psi} &= -d_{3r} d_{3\psi}/r + u_2 d_{1\psi} - u_1 d_{2\psi},\\ \dot{d}_{3z} &= u_2 d_{1z} - u_1 d_{2z}.\end{aligned} \tag{5}$$

For the external normal reaction force we can write $\boldsymbol{f} = f\,\boldsymbol{e}_r$, a positive f corresponding to an inward pointing force per unit length of rod exerted by the cylinder on the rod. This f is determined by the kinematic constraint stipulating that the component of the tangent vector normal to the cylinder must be zero, that is $\dot{r} = d_{3r} \equiv 0$. Eq. (5) then yields the constraint equation

$$\frac{d_{3\psi}^2}{r} + u_2 d_{1r} - u_1 d_{2r} \equiv 0, \tag{6}$$

where from now on r is the constant radius of the cylinder. It turns out to be useful to introduce a new unknown function h defined (up to a constant) by

$$\frac{1}{r} d_{3\psi} n_\psi + f = \dot{h}, \tag{7}$$

and to transform according to

$$\bar{n}_r = n_r - h, \quad \bar{n}_\psi = n_\psi, \quad \bar{n}_z = n_z. \tag{8}$$

Then $\dot{\bar{n}}_r = 0$ and $\dot{\bar{n}}_z = 0$. The end tension requires that $\bar{n}_z = T$ and we can set $\bar{n}_r = 0$ (this fixes the undetermined constant in the definition of h in Eq. (7) and in fact yields the equality $h = n_r$).

The cylindrical constraint implies that there are two degrees of freedom for the director frame $\{\boldsymbol{d}_1, \boldsymbol{d}_2, \boldsymbol{d}_3\}$, instead of the normal three. A useful parametrisation is therefore obtained in terms of two Euler angles, θ and ϕ, as follows:

$$\begin{aligned}\boldsymbol{d}_1 &= \sin\phi\,\boldsymbol{e}_r - \cos\phi\cos\theta\,\boldsymbol{e}_\psi + \cos\phi\sin\theta\,\boldsymbol{e}_z,\\ \boldsymbol{d}_2 &= \cos\phi\,\boldsymbol{e}_r + \sin\phi\cos\theta\,\boldsymbol{e}_\psi - \sin\phi\sin\theta\,\boldsymbol{e}_z,\\ \boldsymbol{d}_3 &= \sin\theta\,\boldsymbol{e}_\psi + \cos\theta\,\boldsymbol{e}_z.\end{aligned} \tag{9}$$

The angle θ measures the deviation from the straight configuration in the cylindrical surface, while ϕ is the internal twist angle of $\boldsymbol{d}_1$ (say) about $\boldsymbol{d}_3$. Thus, a rod with no internal twist, $\phi = 0$, has its $\boldsymbol{d}_1$ lying in the tangent plane to the cylinder, and $\boldsymbol{d}_2$ normal to it, along its entire length. Fig. 1 illustrates the definition of the angles.

By using Eqs. (1)–(4) we can now write down the dimensionless equations for the angles θ and ϕ and the components of force, $\boldsymbol{n}$, and moment, $\boldsymbol{m}$, as follows:

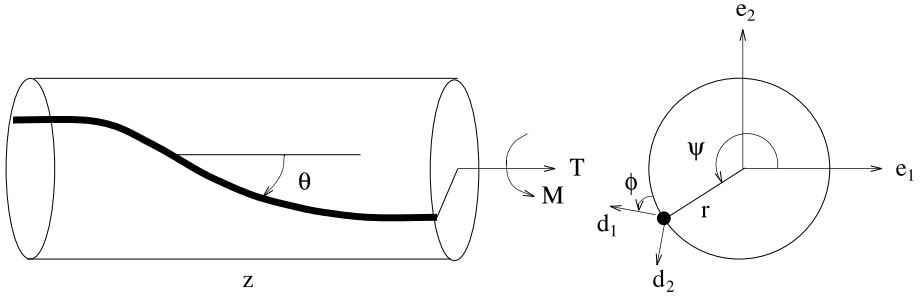

Fig. 1. The angles used to describe the constrained rod.

$$
\begin{aligned}
\dot{x}_2 &= -\frac{1}{\tilde{r}}\,\tilde{h}(x,\theta,\phi)\sin\theta,\\
\dot{x}_4 &= -\frac{1}{m^2}\sin\theta + \frac{1}{m^2}\,x_2\cos\theta + \frac{1}{\tilde{r}}\,x_5\sin\theta,\\
\dot{x}_5 &= -\frac{1}{m^2}\tilde{h}(x,\theta,\phi)\cos\theta - \frac{1}{\tilde{r}}\,x_4\sin\theta,\\
\dot{x}_6 &= \frac{1}{m^2}\tilde{h}(x,\theta,\phi)\sin\theta,\\
\dot{\theta} &= -x_4 - \rho\left(x_4\sin^2\phi - x_5\sin\phi\cos\phi\cos\theta + x_6\sin\phi\cos\phi\sin\theta\right),\\
\dot{\phi} &= (1+v)(x_5\sin\theta + x_6\cos\theta) - \frac{1}{\tilde{r}}\sin\theta\cos\theta.
\end{aligned}
\tag{10}
$$

Here

$$
t = \frac{M}{B_2}\,s, \quad x_2 = \frac{n_\psi}{T}, \quad x_4 = \frac{m_r}{M}, \quad x_5 = \frac{m_\psi}{M}, \quad x_6 = \frac{m_z}{M}, \quad \tilde{h} = \frac{h}{T}, \quad \tilde{f} = \frac{B_2}{MT}\,f, \tag{11}
$$

where T and M are the applied loads. Recall that $n_r = h$ and $n_z = T$ so that no equations for these components are required. The four dimensionless parameters in Eq. (10) are given by

$$
m = \frac{M}{\sqrt{B_2 T}}, \quad \rho = \frac{B_2}{B_1} - 1, \quad v = \frac{B_2}{C} - 1, \quad \tilde{r} = \frac{M}{B_2}\,r. \tag{12}
$$

Note that m is a single load parameter (containing both the tension and the applied moment), ρ is an anisotropy parameter which is zero for rods whose principal bending stiffnesses are equal, v measures the ratio of bending to torsional stiffness (for solid circular rods v equals Poisson's ratio), and $\tilde{r}$ is the dimensionless radius of the cylinder. Without loss of generality we can assume $B_2 \geqslant B_1$ and take ρ to be non-negative. An overdot from now on denotes differentiation with respect to rescaled arclength t.

The constraint (6) reads

$$
x_5\cos\theta - x_6\sin\theta - \rho\left(x_4\sin\phi\cos\phi - x_5\cos^2\phi\cos\theta + x_6\cos^2\phi\sin\theta\right) + \frac{1}{\tilde{r}}\sin^2\theta \equiv 0. \tag{13}
$$

The function $\tilde{h}(x,\theta,\phi)$ in Eq. (10) can now be computed by differentiating Eq. (13) and inserting Eq. (10). The dimensionless reaction force $\tilde{f}$ is then found by differentiating $\tilde{h}$ and using the rescaled version of Eq. (7). For the anisotropic rod ($\rho \neq 0$) this gives very long expressions which we shall omit here. Expressions for the isotropic case can be found in van der Heijden (2001).

Once a solution to Eq. (10) has been found, the actual shape of the rod is obtained by solving the centreline equation in Eq. (1), which can be rewritten as

$$
\dot{\psi} = \frac{1}{\tilde{r}}\sin\theta, \qquad \dot{z} = \cos\theta. \tag{14}
$$

To express the solution in fixed Cartesian co-ordinates (x,y,z) one finally takes

$$
x = \tilde{r}\cos\psi, \qquad y = \tilde{r}\sin\psi. \tag{15}
$$

For any choice of parameters $(m,\rho,v,\tilde{r})$, Eq. (10) has the trivial solution given by

$$
x_2 = 0, \quad x_4 = 0, \quad x_5 = 0, \quad x_6 = 1, \quad \theta = 0, \quad \dot{\phi} = 1 + v, \tag{16}
$$

implying $\tilde{h} = 0$. Here, in obtaining $x_6 = 1$, the moment boundary condition has been used for the first time. The solution (16) represents the straight but twisted rod in tension, and in this paper we shall be concerned mainly with localised rod solutions which tend to this straight configuration towards the ends. Making the

idealisation of an infinitely long rod, this means that we are looking for homoclinic orbits to the periodic solution (16) of Eq. (10).

2.2. Symmetries and first integrals

Symmetries play an important role in determining multiplicities of solutions (see also van der Heijden and Thompson (1998) and references therein for further interpretations of (reversing) symmetries in the context of rod statics). The system (10) has the following two reversing symmetries:

$$R_1 : (x_2, x_4, x_5, x_6, \sin\theta, \sin 2\phi) \to (x_2, -x_4, x_5, x_6, \sin\theta, -\sin 2\phi), \quad t \to -t \ (h \to -h), \tag{17}$$

$$R_2 : (x_2, x_4, x_5, x_6, \sin\theta, \sin 2\phi) \to (-x_2, x_4, x_5, -x_6, -\sin\theta, \sin 2\phi), \quad t \to -t \ (h \to -h). \tag{18}$$

Note, however, that the reversing symmetry R_2 is broken by our boundary conditions, i.e., by the applied wrenches (the integral I_1 below would have to be zero). Therefore, we only have R_1-reversibility, and solutions will be either R_1-reversible themselves or come in symmetric pairs.

The R_1 reversibility can be broken down further by specifying whether reflection of the ϕ-angle is about 0, $\pi/2$, π or $3\pi/2$. When such detailed information is required, R_1-symmetric solutions will be denoted accordingly by $R_1^{\phi_0}$, where $\phi_0 \in \{0, \pi/2, \pi, 3\pi/2\}$ is the value of ϕ in the fixed point set of R_1.

We also have the following symmetry:

$$Z : \phi \to \pi + \phi \quad (h \to h), \tag{19}$$

which corresponds to a 180° rotation of the cross-section of the rod. Note that $Z = R_1^0 R_1^{\pi/2} = R_1^{\pi} R_1^{3\pi/2}$.

The system (10) also has two first integrals. One immediately follows by inspection:

$$I_1 = \tilde{r}x_2 + m^2 x_6 = \text{constant}. \tag{20}$$

Since x_2 is the component of internal force in the circumferential direction, this integral is seen to express axial moment balance. The second integral is given by $\mathscr{H} = \frac{1}{2}B_1 u_1^2 + \frac{1}{2}B_2 u_2^2 + \frac{1}{2}C u_3^2 + \boldsymbol{n} \cdot \boldsymbol{d}_3$, which, when interpreted properly, is the Hamiltonian. In dimensionless form it reads

$$I_2 = \frac{1}{2}(1+\rho)(x_4 \sin\phi - x_5 \cos\phi \cos\theta + x_6 \cos\phi \sin\theta)^2 + \frac{1}{2}(x_4 \cos\phi + x_5 \sin\phi \cos\theta - x_6 \sin\phi \sin\theta)^2 + \frac{1}{2}(1+\nu)(x_5 \sin\theta + x_6 \cos\theta)^2 + \frac{\cos\theta}{m^2} + \frac{x_2 \sin\theta}{m^2} = \text{constant}. \tag{21}$$

In the case of an isotropic rod (i.e., $\rho = 0$), the conserved twist u_3 provides a third integral which can be written as

$$I_3 = x_5 \sin\theta + x_6 \cos\theta = \text{constant} \quad (\rho = 0). \tag{22}$$

2.3. The isotropic rod

As shown in van der Heijden (2001), the three integrals I_1, I_2, I_3 make the isotropic case completely integrable. In fact, system (10) can be reduced to the following one-degree-of-freedom equivalent oscillator:

$$\tfrac{1}{2}\dot{\theta}^2 + V(\theta) = H, \tag{23}$$

where

$$V(\theta) = \frac{\cos\theta}{m^2} + \frac{K_1 \sin\theta}{\tilde{r}m^2} - \frac{K_3 \sin\theta\cos\theta}{\tilde{r}} + \frac{\cos^2\theta}{\tilde{r}^2} - \frac{\cos^4\theta}{2\tilde{r}^2}, \tag{24}$$

$$H = K_2 - \frac{1}{2}K_3^2(1+\nu) + \frac{1}{2\tilde{r}^2}. \tag{25}$$

Here, K_1, K_2 and K_3 are the values of the integrals I_1, I_2 and I_3, respectively, which follow from the boundary conditions. For homoclinic boundary conditions we have to take K_1 and K_3 to be those of the trivial solution (16):

$$K_1 = m^2, \quad K_3 = 1. \tag{26}$$

K_2 is not prescribed and parametrises the energy H of the equivalent oscillator.

Phase portraits of the oscillator (23), subject to Eq. (26), are given in van der Heijden (2001) where the isotropic case is studied in detail, (but see also Fig. 13). The straight solution (16) is represented by a saddle point at the origin. Other fixed points of Eq. (23) are given by non-zero solutions of

$$V'(\theta) = 0, \tag{27}$$

and correspond to helical solutions with pitch angle $\pi/2 - \theta$ and axial wavelength λ given by

$$\lambda = \frac{2\pi\tilde{r}}{|\tan\theta|}. \tag{28}$$

By Eq. (14), the helix is right-handed if $0 < \theta < \pi/2$ or $-\pi < \theta < -\pi/2$, and left-handed if $\pi/2 < \theta < \pi$ or $-\pi/2 < \theta < 0$; it is in tension if $|\theta| < \pi/2$, and in compression if $\pi/2 < |\theta| < \pi$. Helical solutions have a constant distributed reaction force $\tilde{f}$.

The principal new ingredient in the reduced 'dynamics' (compared to the free-rod case of van der Heijden and Thompson (2000)) is the occurrence, at critical values of the load $m = m_{c_i}$, of heteroclinic orbits connecting the origin to a non-trivial saddle. The number of these critical loads depends on the parameter $\tilde{r}$, the dimensionless radius of the cylinder: for small enough $\tilde{r}$ ($\tilde{r} < 0.964823$) there are two critical points, while for larger $\tilde{r}$ only the lower-m one persists. The physical implication is that a rod held at these critical loads is infinitely sensitive to changes in load and wants to collapse into a helix. In a load–deflection diagram this yields curves that asymptote to infinity at these critical loads. The reader may care to look ahead to Figs. 4 and 5 (for $\tilde{r} = 0.8$) in which dotted curves show the end shortening against the load m for localised solutions of the isotropic rod. The difference between the two figures is the direction of departure of the homoclinic orbit from the saddle point at the origin ($\delta > 0$ or $\delta < 0$, in the following section's terminology). The saddle points are located such that for $\delta > 0$ (Fig. 4) continuation of the homoclinic orbit reveals both critical points, while for $\delta < 0$ (Fig. 5) only the lower-m one shows up.

Note that for this isotropic case each of these critical loads is reached monotonically upon increasing end shortening. As we shall see in the next section, one of the key differences that the introduction of anisotropy $\rho \neq 0$ makes is that the path oscillates as it rises in end shortening. Thus, instead of vertical asymptotes at a unique critical load, we get 'wiggly towers' that oscillate between two different load values.

3. Numerical results for the anisotropic rod

From general dynamical systems theory we expect the equations for the anisotropic rod ($\rho \neq 0$) in general to be non-integrable (I_3 no longer being a first integral). This means that a reduction of Eq. (10) to a planar oscillator is no longer possible. The equation for the twist angle ϕ couples to the θ equation, and the trivial solution (16) has to be regarded as a periodic solution, of period $T_p = 2\pi/(1+\nu)$, in a 6D phase space.

Furthermore, we should expect the loss of integrability generically to be accompanied by the emergence of spatial chaos described by Smale horseshoes (see Mielke and Holmes, 1988). In particular, alongside surviving 'primary' homoclinic orbits, we expect the presence of infinitely many multi-loop homoclinic

orbits to the trivial periodic solution (a result known as 'Devaney's Theorem'). In this section we will verify this by numerically computing families of homoclinic orbits making use of the combination of a shooting method and numerical continuation. We closely follow the methods we used for the planar case in van der Heijden et al. (1999b) to which the reader is referred for more details.

3.1. The shooting method

The idea is to define a two-point boundary-value problem that yields approximate localised solutions on a truncation of the full (infinite) arclength of the rod. Standard numerical methods for homoclinic solutions must be adapted to deal with the constraint and the fact that the trivial solution is a periodic orbit (16) of the system (10). Linearisation about this trivial periodic solution at all parameters of interest reveals one stable, one unstable and four unit Floquet multipliers (zero eigenvalues). Therefore to specify that the solution we seek should be localised, we choose a left-hand boundary condition that places solutions in the 1D unstable eigenspace. Specifically, we truncate the arclength interval to $[-\mathscr{T},0]$ and take

$$\boldsymbol{x}(-\mathscr{T}) = p + \delta\varepsilon\boldsymbol{v}, \quad \text{where} \quad \boldsymbol{x} = (x_2, x_4, x_5, x_6, \theta, \phi) \ \text{and} \ p = (0,0,0,1,0,0), \tag{29}$$

where $\boldsymbol{v}$ is an unstable eigenvector, δ and $\mathscr{T} \gg 1$ are as yet unknown shooting parameters and ε is small and fixed. Note that the choice of p fixes the phase of the trivial periodic solution.

Because our system is reversible, an appropriate right-hand boundary condition is to place the solution in the symmetric section (fixed point set) $S_1^{\phi_0}$ of the reversing symmetry $R_1^{\phi_0}$, i.e.,

$$S_1^{\phi_0} : x_4(0) = 0, \quad \phi(0) = \phi_0 (\mathrm{mod}\ 2\pi). \tag{30}$$

In order to compute the configuration of the rod we also solve Eq. (14) subject to the initial conditions

$$\psi(-\mathscr{T}) = 0, \quad z(-\mathscr{T}) = 0. \tag{31}$$

Then the end shortening d can be approximated by

$$d = 2(\mathscr{T} - z(0)), \tag{32}$$

the factor of 2 appearing because $\mathscr{T}$ represents half the length of the rod.

Eqs. (10) and (14) with initial condition (29) and (31) form a well-defined shooting problem for locating homoclinic orbits, provided $\mathscr{T}$ is sufficiently large and ε sufficiently small. Varying the two parameters δ and $\mathscr{T}$ we can satisfy the right-hand boundary conditions (30). Note that although δ and $\mathscr{T}$ are not independent, homoclinic orbits occur at isolated values of these shooting parameters. This technique for finding homoclinic orbits to periodic orbits is akin to that in Bai et al. (1996). Effectively, $\delta \in (\delta_0, \delta_1)$, for some positive constants $\delta_{0,1}$, parametrises distinct solutions in one component of the local unstable manifold of p, and $\mathscr{T}$ parametrises time along one such trajectory.

We note here that the initial conditions (29), inevitably, will not satisfy the cylindrical constraint *exactly*. That is, the left-hand side of Eq. (13), which we recall is $\dot{\boldsymbol{d}}_{3'}$ $(= \ddot{\boldsymbol{r}})$, will not be exactly zero, and the error may grow during numerical integration. To prevent this drift, i.e., the slowly moving away of the solution from the constraint manifold, one might want to add suitable constraints to the system of equations, introduce Lagrange multipliers, and solve the problem as a differential–algebraic equation (DAE), for which good numerical solvers are available (see, e.g., Hairer et al., 1996). However, since we are not interested in the asymptotic behaviour of solutions but rather in computing solutions over truncated arclength intervals, good results can be obtained by solving Eq. (10) as an ODE. Thus, although $\mathscr{T}$ increases as $\varepsilon \to 0$, we find that by taking $\varepsilon = 10^{-5}$ integration times for the solutions to be presented (typically in the range 25–40) are such that drift of solutions off the cylinder is of no real concern: in the worst-case shooting we found the constraint (13) satisfied to within 6×10^{-9}, while a more typical error was 10^{-10}. (Incidentally, by working with $\tilde{\boldsymbol{h}}$ in Eq. (10), rather than $\tilde{\boldsymbol{f}}$ directly, we have lowered the index of the DAE by one, the reason for

doing so being that the lower-index formulation behaves far better in the numerical computations when it comes to preserving the constraint. For completeness let us here point out that the original problem (1) with the constraint $r = \text{const.}$ constitutes an index-4 DAE. The reduction in Section 2.1, with the centreline equations (14) decoupling, turns that original problem into an index-2 DAE for the constraint $\dot{d}_{3r} = 0$. The transformation to $\tilde{h}$ finally yields the system (10) with the constraint (13), which forms an index-1 DAE.)

At fixed parameter values, solutions to the two-point boundary value problem are sought by a shooting method that uses the variational equations and Newton's method to solve for δ and $\mathscr{T}$. Solutions to the initial-value problem at each iteration are obtained using a highly accurate numerical integration routine (the eighth-order Runge–Kutta code `DOP853` as described in Hairer et al. (1993)) with local error tolerance 10^{-12}. For continuation of solutions as one parameter varies, we use the code AUTO (see, e.g., Doedel et al., 1997) that uses orthogonal collocation allied to pseudo-arclength continuation.

3.2. Primary localised solutions

We now present results initially for the fixed parameter values $v = 1/3$, $\tilde{r} = 0.8$, $\rho = 0.2$ and $m = 1.5$ (for this value of $\tilde{r}$ the isotropic rod has two critical loads and therefore the richest possible bifurcation behaviour, cf. Section 2.3). For the unstable eigenvector $\boldsymbol{v}$ in Eq. (29) at these parameter values we use the unit vector

$$\boldsymbol{v} = (0, -0.26812153, 0.42606424, 0, 0.42181235, -0.75409180), \tag{33}$$

obtained by integrating over one period $T_p = 2\pi/(1+v) = 4.71238898$, the linearised equations about the trivial periodic solution (16). Tables 1 and 2 give shooting data for the two different homoclinic orbits to the origin, obtained by taking $\delta > 0$ and $\delta < 0$, respectively. Both sets represent two physically distinct solutions only: the R_1^0- and R_1^π-symmetric solutions are physically identical, as are the $R_1^{\pi/2}$- and $R_1^{3\pi/2}$-symmetric solutions. The difference in the $\mathscr{T}$ values of both members of either pair is $T_p/2$, as dictated by Z-symmetry (one solution simply has tails half a period longer than those of the other one in the pair to accommodate an extra half turn of the twist angle ϕ at the midpoint).

Physical shapes and the corresponding reaction forces $\tilde{f}$ for the first two solutions in Tables 1 and 2 are displayed in Figs. 2 and 3. Note that in these figures, as in figures to come, the scale in the z direction is considerably different from that in the x and y directions. Also note that although the shapes of the two solutions in Fig. 2 are fairly similar, the reaction forces are not: the R_1^0-symmetric solution requires a markedly stronger force than the $R_1^{\pi/2}$-symmetric solution.

Continuation results for the primary homoclinic solutions are depicted in Fig. 4 ($\delta > 0$) and Fig. 5 ($\delta < 0$). Here we have used AUTO to trace load–deflection diagrams by allowing m to vary and monitoring the value of d (although of course from a physical point of view, we can interpret the resulting diagrams as if either d or m were the controlled parameter). The first observation from both figures is that the solution curves of the anisotropic rod oscillate about those of the isotropic rod as they approach the critical loads m_c. Note that in Fig. 4 this occurs for both of the critical loads although, as shown by the inset, the

Table 1
Shooting data for primary homoclinic orbits with $\delta > 0$ ($v = 1/3$, $\tilde{r} = 0.8$, $\rho = 0.2$)

Reversibility	$m = 1.5$		$m = 2.0$	
	δ	$\mathscr{T}$	δ	$\mathscr{T}$
R_1^0	0.00144662805	30.2490751	0.128617313	29.5796290
$R_1^{\pi/2}$	0.000726766235	31.4923817	0.0698582037	30.7599981
R_1^{π}	0.000279533858	32.6052696	0.0374831080	31.9358240
$R_1^{3\pi/2}$	0.000140434004	33.8485762	0.0203588515	33.1161926

Table 2
Shooting data for primary homoclinic orbits with $\delta < 0$ ($v = 1/3$, $\tilde{r} = 0.8$, $\rho = 0.2$, $m = 1.5$)

Reversibility	δ	$\mathscr{T}$
R_1^0	−0.00125151582	27.4190902
$R_1^{\pi/2}$	−0.000649375708	28.8490183
R_1^{π}	−0.000241832057	29.7752847
$R_1^{3\pi/2}$	−0.000125479728	31.2052128

oscillations in m have a much smaller amplitude about the higher critical load m_{c_2}. In fact, at this higher critical load there are a total of four branches that 'wiggle up the tower'. The process repeats up to infinite d but here is truncated due to the finiteness of $\mathscr{T}$. Upon taking longer truncation intervals, the computations could be continued up to higher d with the slope of the end shortening versus m segments of each oscillation getting successively steeper. The process that is occurring as the curves oscillate, which can be seen in the insets showing the 3D rod shapes, is qualitatively similar to what happens in the isotropic case: as the critical load is approached, the rod gains more and more helical turns until in the limit it approaches a (pair of) heteroclinic connections to a periodic helical state.

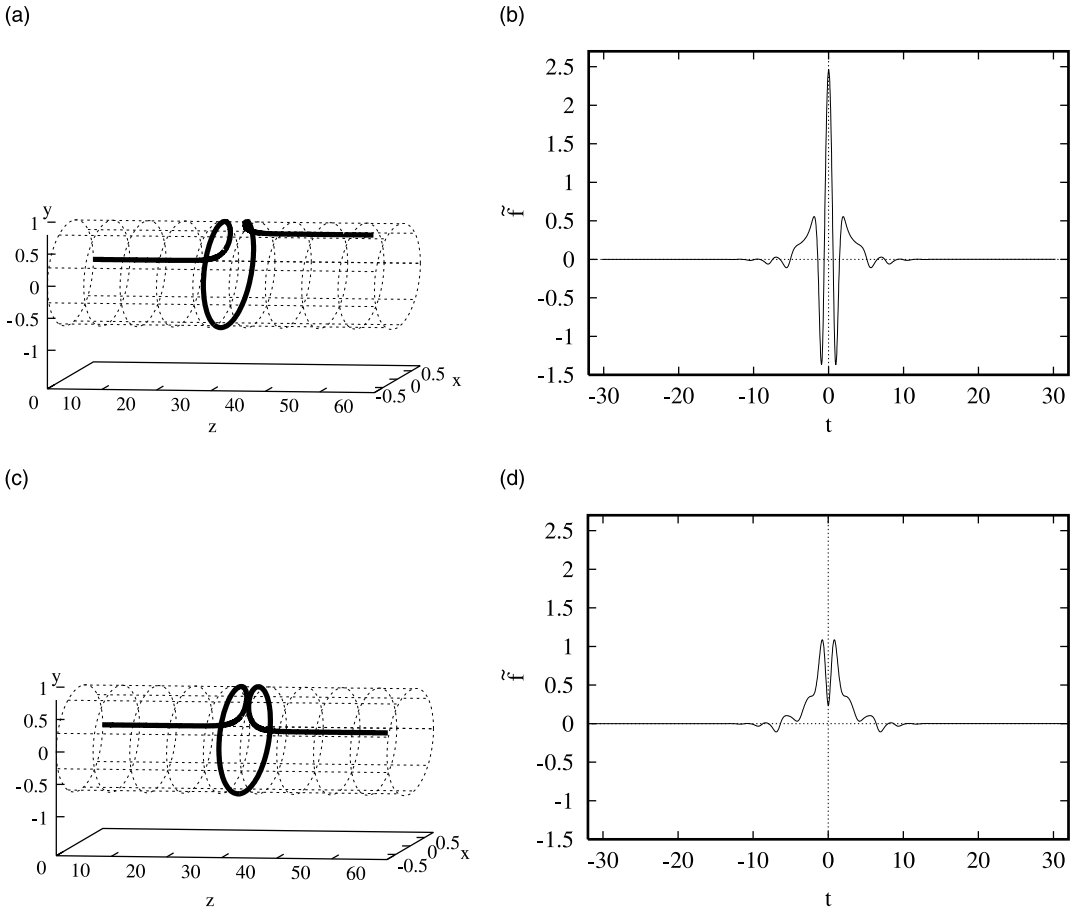

Fig. 2. The first two primary homoclinic solutions of Table 1 and their corresponding reaction forces $\tilde{f}$ ($v = 1/3$, $\tilde{r} = 0.8$, $\rho = 0.2$, $m = 1.5$).

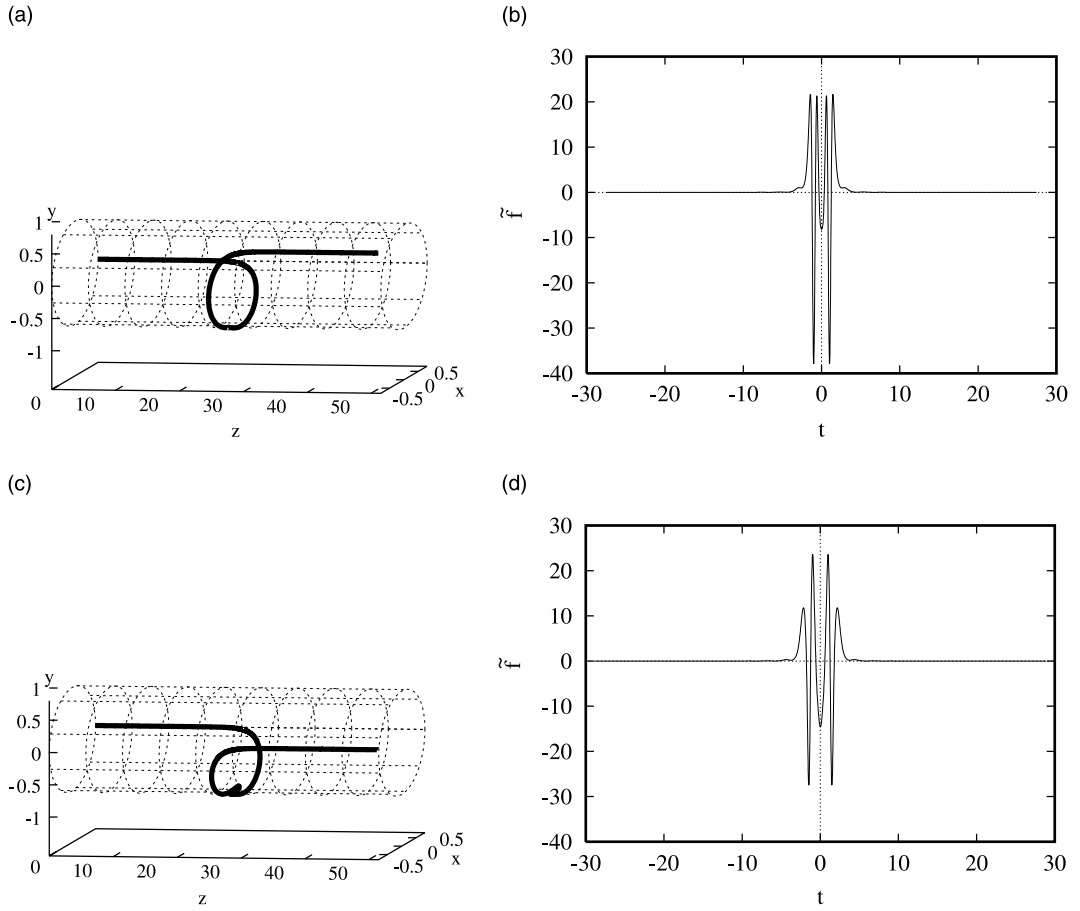

Fig. 3. The first two primary homoclinic solutions of Table 2 and their corresponding reaction forces $\tilde{f}$ ($v = 1/3$, $\tilde{r} = 0.8$, $\rho = 0.2$, $m = 1.5$).

Similar computations for different values of $\rho > 0$ have revealed a qualitatively similar load–deflection diagram, with the width of the oscillations in m increasing as ρ is increased. (Look ahead, for example, to the dotted curves in Figs. 8 and 9 which are for various ρ values.)

This 'snaking' behaviour of paths of localised solutions about a critical load has recently been observed in a number of elastic structures which have a characteristic destiffening (subcritical) post-buckling characteristic combined with the propensity to restabilise at larger amplitude. A classic example is the axially-compressed cylindrical shell. See Hunt et al. (1999), and (2000), where an explanation of this phenomenon is given via a variety of dynamical systems, variational and energy arguments (see also Section 5). Mathematically it is typically to be expected in Hamiltonian systems featuring a heteroclinic tangle between the stable and unstable manifolds of a saddle-type equilibrium and periodic orbit. This process is described in detail in Figs. 3 and 4 of Hunt et al. (1999). Given that our system has a 6D phase space but two integrals, it is equivalent to the 4D phase space in which this process was originally described. Here, though, unlike in the previous systems where the heteroclinic tangle arises from a degenerate Hamiltonian–Hopf bifurcation, the tangle arises as the heteroclinic orbit of the underlying integrable system gets destroyed by non-zero ρ. In the theory, which is perfectly borne out by our numerical results, the left and right fold

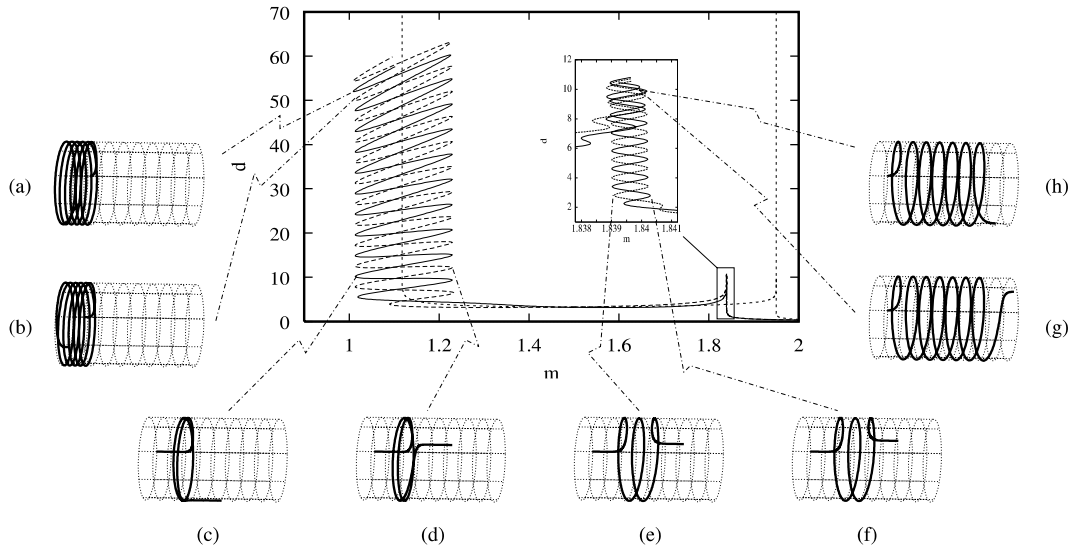

Fig. 4. End shortening d against load m for an anisotropic rod. Shown are curves for the R_1^0-symmetric (—) and $R_1^{\pi/2}$-symmetric (- - -) primary homoclinic solutions of Table 1. The dotted curve represents data for the isotropic rod ($\nu = 1/3$, $\tilde{r} = 0.8$, $\rho = 0.2$).

points along the snaking curves approach asymptotic values which correspond to the m values at which initial and final heteroclinic tangencies occur. For loads in between these limiting values there exist infinitely many distinct localised solutions.

Fig. 6 shows in more detail what a solution some distance up the left-hand wiggly tower in Fig. 4 looks like, in comparison with the corresponding isotropic-rod solution at the same end shortening d. The anisotropic rod is not a true helix in the middle, but θ varies only slightly and the shape is not noticeably different from that of the isotropic rod (not shown). However, the reaction force $\tilde{f}$ (constant for a true helix) is seen to vary strongly along the nearly helical part. Note that $\tilde{f}$ is predominantly negative, corresponding to an outward pointing reaction force. Also note from the shape in Fig. 6(c) that the central helical part is held in compression.

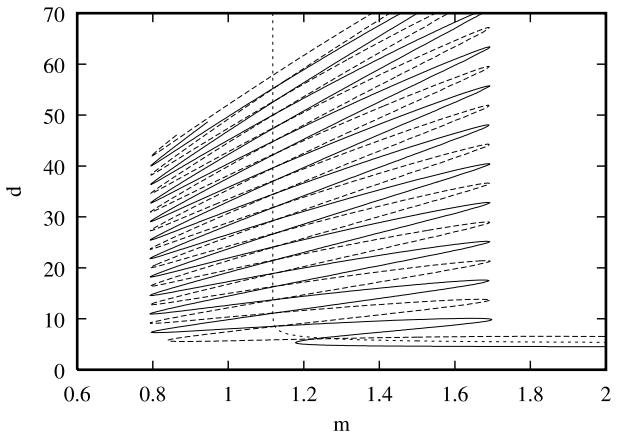

Fig. 5. End shortening d against load m for an anisotropic rod. Shown are curves for the R_1^0-symmetric (—) and $R_1^{\pi/2}$-symmetric (- - -) primary homoclinic solutions of Table 2. The dotted curve represents data for the isotropic rod ($\nu = 1/3$, $\tilde{r} = 0.8$, $\rho = 0.2$).

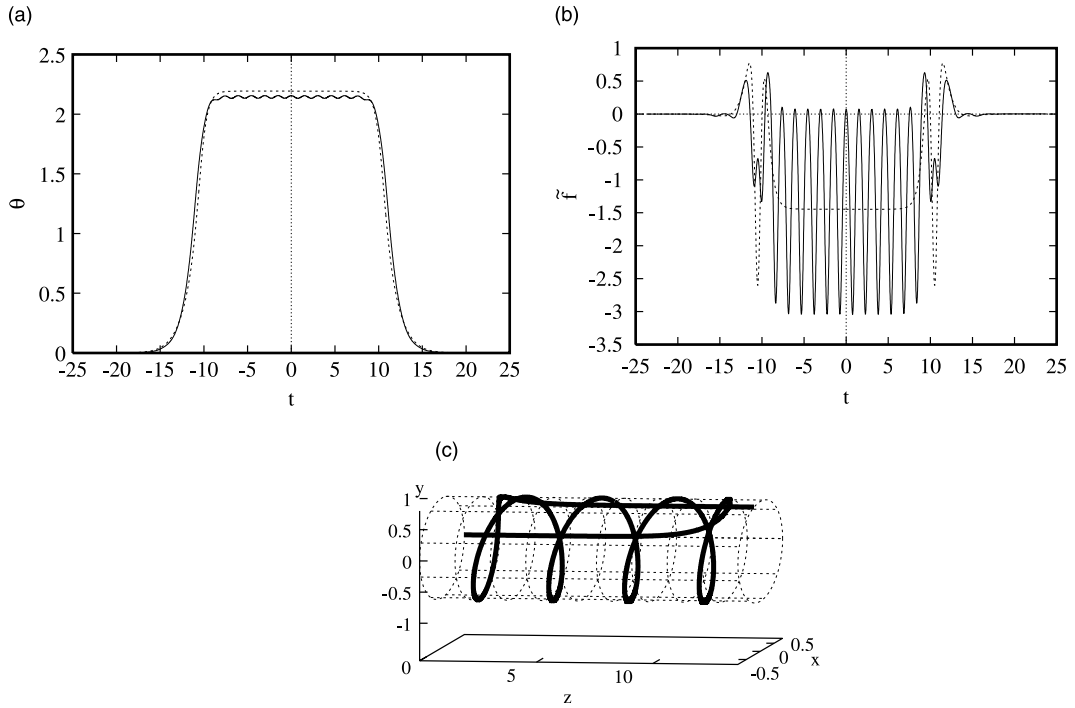

Fig. 6. Example of a solution along the R_1^0 curve of Fig. 4 ($m = 1.013$, $d = 33.62$). Dotted curves are for the corresponding isotropic rod at the same value of the end shortening d ($\nu = 1/3$, $\tilde{r} = 0.8$, $\rho = 0.2$).

Table 3
Shooting data for two-loop homoclinic orbits ($\nu = 1/3$, $\tilde{r} = 0.8$, $m = 1.5$)

Reversibility	$\rho = 0.2$		$\rho = 0.008$	
	δ	$\mathscr{T}$	δ	$\mathscr{T}$
R_1^0	0.00748013657	36.9425795	0.0159331395	36.7661704
$R_1^{\pi/2}$	0.00376342739	38.2525128	0.00753907613	37.9427739
R_1^{π}	0.00144539682	39.2987740	0.00330181761	39.1223649
$R_1^{3\pi/2}$	0.000727212097	40.6087073	0.00156231937	40.2989684

Broadly speaking we see that for the case of primary localised modes there is a strong similarity with the isotropic case. The overall feature is that there is a critical load value (given now by the left-hand limit point (LP) of the wiggly tower) beyond which there are no localised responses possible. Section 4 below is dedicated to a more physical interpretation of this behaviour.

3.3. Multi-loop solutions

A strong difference with the isotropic case is that for non-zero ρ we also find a whole multitude of multi-loop homoclinic solutions that do lie on the primary bifurcation curves depicted in Figs. 4 and 5. Table 3 presents, for two different ρ values, shooting data for four particular two-loop solutions that do not lie on a primary branch. The corresponding solutions are plotted in Fig. 7. Figs. 8 and 9 give continuation results.

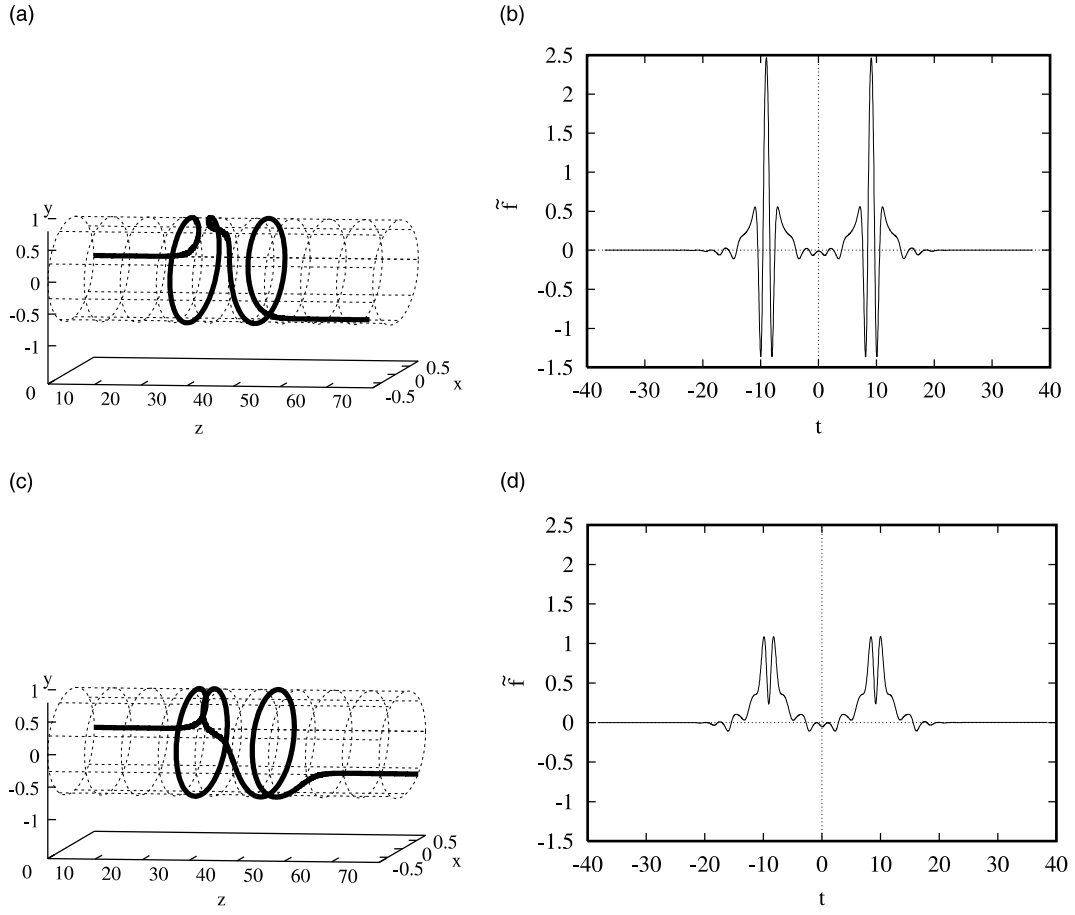

Fig. 7. The R_1^0-symmetric (top) and $R_1^{\pi/2}$-symmetric (bottom) two-loop homoclinic solutions of Table 3 and their corresponding reaction forces $\tilde{f}$ ($v = 1/3$, $\tilde{r} = 0.8$, $\rho = 0.2$, $m = 1.5$).

The former is for $\rho = 0.008$ and shows that for small enough ρ the two-loop homoclinic orbits of Table 3 live on separate closed bifurcation curves. Note that there exists a separate closed curve of two-loops to the left of those for the two-loops of Table 3, and a further branch of two-loops to the right. This latter branch runs up the right tower. Solutions on the flanking branches are qualitatively similar to those on the central closed curve of two-loops. From Fig. 9 it is seen that, at larger ρ, the bifurcation curves merge and start interacting with the wiggly towers of primary solutions. At $\rho = 0.2$ the central two-loop curve has connected, via a transcritical bifurcation, to the right tower so that the curve of two-loops follows a similar snaking sequence as the primary curve, although being quite distinct from it.

The behaviour near the left-hand wiggly tower is different upon increase of ρ. The left isola is drawn closer to the expanding wiggles of the tower, but in so doing it keeps its integrity. In Fig. 9(a) for $\rho = 0.2$, the isola appears to touch the main curve of two-loops and one might imagine that at a slightly higher ρ value there would be a transcritical bifurcation and the two would merge. However, as panel (b) shows, even for $\rho = 1$ this has yet to take place, although, as the inset shows, to see that the two curves are really distinct and do not touch requires a high level of numerical accuracy. Similar nearly touching isolae exist higher up the wiggly tower. Meanwhile, at $\rho = 1$ the right tower has disappeared.

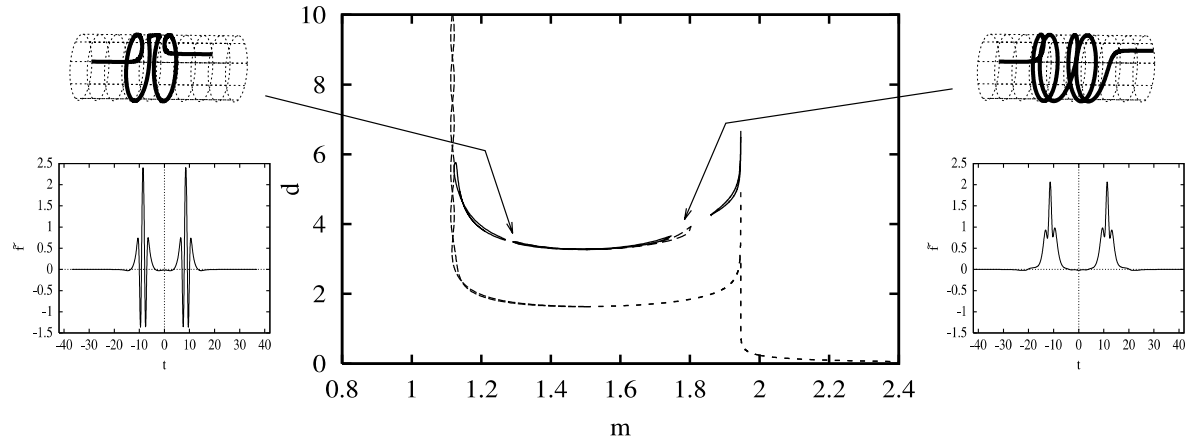

Fig. 8. Continuation data for the R_1^0-symmetric (—) and $R_1^{\pi/2}$-symmetric (- - -) two-loops of Table 3. An additional closed curve of R_1^0-symmetric two-loops is shown to the left, and a further branch of R_1^0-symmetric two-loops is shown to the right. Dotted lines represent primary orbit data. Displayed are $R_1^{\pi/2}$-symmetric solutions at $m = 1.3$ (left) and $m = 1.8$ (right) ($v = 1/3$, $\tilde{r} = 0.8$, $\rho = 0.008$).

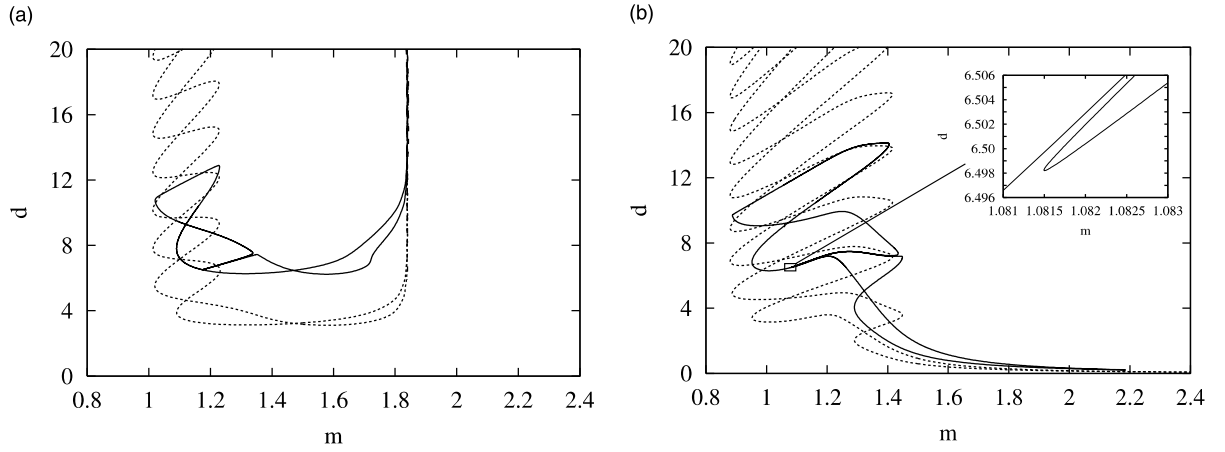

Fig. 9. Continuation data for the R_1^0-symmetric two-loop of Table 3 superimposed on the primary orbit curves ($\cdots$) for (a) $\rho = 0.2$ and (b) $\rho = 1$ ($v = 1/3$, $\tilde{r} = 0.8$).

Fig. 10 shows curves of LP obtained from a two-parameter continuation of the fold points for the R_1^0-symmetric solution. Note that the crossing of the two curves near $\rho = 0.025$ does not imply a bifurcation since the two folds are occurring for different values of d.

The behaviour of isolae of solutions interacting and merging with wiggly towers of solutions is superficially reminiscent of the zipper behaviour observed in a 4D system, from rotordynamics, in which Šil'nikov bifurcations are present (van der Heijden, 2000). There, isolae of *periodic* solutions merge in transcritical bifurcations to form a wiggly tower. Here, isolae of *homoclinic* orbits perform a similar act.

Clearly we have only scratched at the surface of all the possible multi-loop localised states that occur for this model. For instance, by Devaney's Theorem we expect there to be infinitely many solutions for each $m > m_{c_1}$. For the rest of this paper, though, we shall focus on the primary homoclinic solutions, since, at least away from the wiggly towers, these are likely to be the minimum-energy configurations.

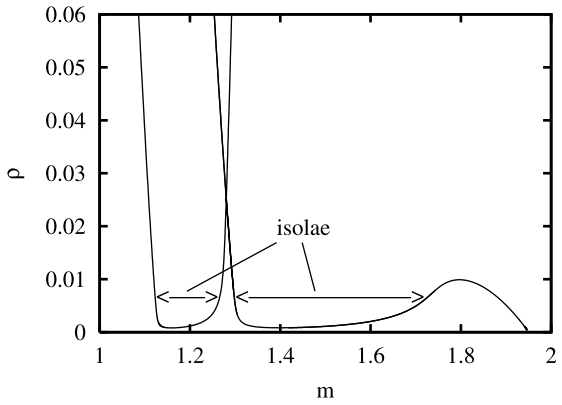

Fig. 10. Some LP curves for R_1^0-symmetric two-loops ($v = 1/3$, $\tilde{r} = 0.8$).

4. The Maxwell load

Recently, the concept of a critical so-called ML has been advanced as a tool in studying buckling problems of characteristic destiffening-restiffening type (see Hunt et al. (2000), and also Peletier (2001) for a more rigorous treatment). We shall now assess how well this concept relates to the wiggly curves of Fig. 4. Among several equivalent definitions is that the ML is defined to be the load at which a periodic orbit has the same total potential energy and value of the Hamiltonian as the trivial straight solution. Hence this is the load where a structure is keen to 'jump' into the periodic mode and it also corresponds in phase space to where a heteroclinic connection between these states is allowed. We recall that in the isotropic case heteroclinic connections between the saddle at the origin and a non-trivial saddle (corresponding to a helix) occurred at certain critical loads m_{c_i}. Both these saddles strictly become periodic orbits of the system in the anisotropic case, so the non-trivial periodic orbit is a candidate for the minimum-energy solution occurring at a certain critical ML somewhere near m_{c_i}.

We will verify this by monitoring the total potential energy along a wiggle high up on the snaking towers for the R_1^0-symmetric primary homoclinic orbit shown in Fig. 4. Solutions sufficiently high up on these towers will spend long enough near the non-trivial periodic orbit to estimate the total potential energy in one period of this solution. The total potential energy, over one period P, can be written as

$$L = \int_0^P (U + U_s + U_r)\,\mathrm{d}t, \tag{34}$$

where

$$\begin{aligned} U &= \tfrac{1}{2}(1+\rho)(x_4\sin\phi - x_5\cos\phi\cos\theta + x_6\cos\phi\sin\theta)^2 + \tfrac{1}{2}(x_4\cos\phi + x_5\sin\phi\cos\theta \\ &\quad - x_6\sin\phi\sin\theta)^2 + \tfrac{1}{2}(1+v)(x_5\sin\theta + x_6\cos\theta)^2, \\ U_s &= \frac{1-\cos\theta}{m^2}, \\ U_r &= -(\dot{\phi}+\dot{\psi}), \end{aligned} \tag{35}$$

with

$$\dot{\phi} = (1+v)(x_5\sin\theta + x_6\cos\theta) - \frac{1}{\tilde{r}}\sin\theta\cos\theta, \qquad \dot{\psi} = \frac{1}{\tilde{r}}\sin\theta. \tag{36}$$

This U physically represents the strain energy, while the integrals of U_s and U_r are, respectively, the work done through the end shortening and the end rotation. It can be verified that for $\rho = 0$ the integrand of L

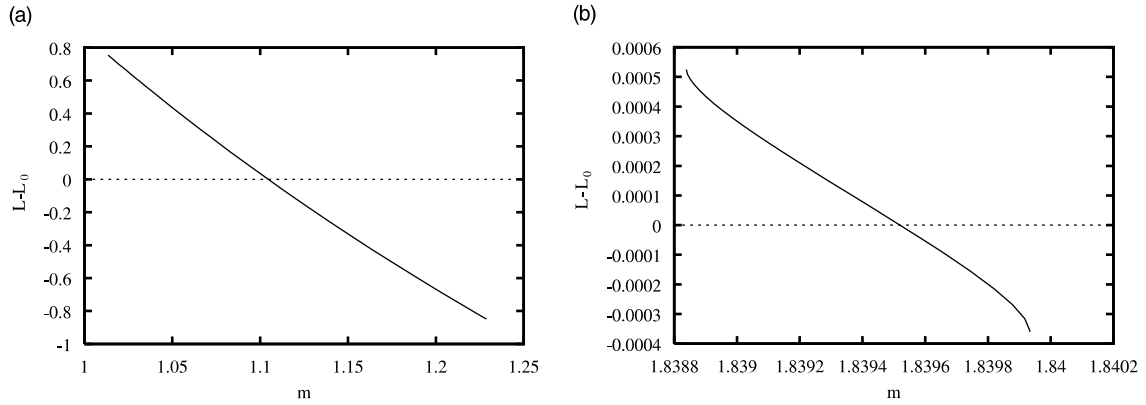

Fig. 11. Total potential energy difference $L - L_0$ as a function of the load m along a wiggle of the snaky curves for the R_1^0-symmetric primary homoclinic solution shown in Fig. 4. (a) is for the left, (b) for the right tower in Fig. 4. Intersections with the horizontal axis signify critical ML ($v = 1/3$, $\tilde{r} = 0.8$, $\rho = 0.2$).

gives a Lagrangian for the equivalent oscillator (23). We note that the total potential energy of the trivial solution (16) (period normalised to one) is

$$L_0 = -\tfrac{1}{2}(1 + v). \tag{37}$$

The results are shown in Fig. 11 which depicts the result of numerical continuation in m of the periodic orbit at the top of both wiggly towers of Fig. 4. For both, the total potential energy difference $L - L_0$ is found to go through zero, the m value of which defines the ML. Fig. 12 shows how this ML and the asymptotic LP (folds) of the low-m wiggly tower vary with ρ. At $\rho = 0$, the ML coincides with the heteroclinic bifurcation value $m = m_{c_1} = 1.117658$. Then, as ρ increases, the ML varies only slightly, but the fold points are seen to open out into a wedge-shaped region.

Let us now try to motivate physically the significance of these results for the case that the tension is varied rigidly (i.e., controlled end shortening) for a prescribed end twist. This might, for example be the situation for an oilwell drill string being quasi-statically introduced into a borehole. The ML represents where the near-helical solutions (such as the one shown in Fig. 6) corresponding to the non-trivial periodic solutions become energetically favourable to the trivial state and hence the rod is happy under increasing end shortening to coil up at this point. For the isotropic case this coiling process is continuous and hence the ML coincides with the

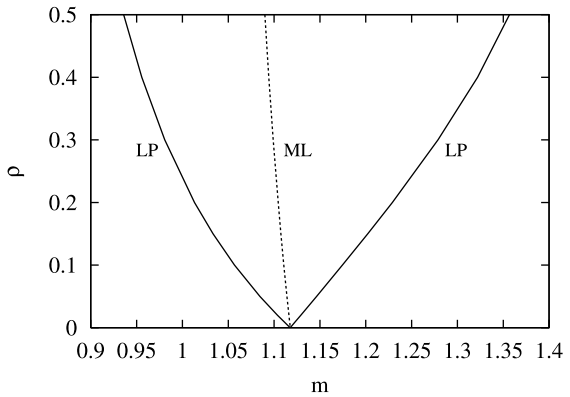

Fig. 12. Curves of asymptotic LP and ML in the m–ρ parameter plane ($v = 1/3$, $\tilde{r} = 0.8$).

critical load m_{c_i}. In the non-isotropic case, however, appealing to arguments as in Peletier (2001), the presence of the wiggles suggests that the rod would undergo a sequence of dynamic jumps (horizontally in Fig. 4) as the rod continually prefers energetically to be on the limb of the wiggly tower that is closest to the ML.

5. Discussion

This paper has given the general formulation of a twisted rod constrained to lie in permanent contact with a rigid cylinder. This is intended as an idealisation of the problem of a rod constrained to lie inside a cylinder with the consequent possibility of lift-off at points where the reaction force is zero and starts to point outwards rather than in. The latter is of course much harder and not amenable to the simple treatment given here. Nevertheless, we believe that the permanent contact problem is likely to give significant insight into the more realistic case. This is especially so since there is evidence that drill strings in a circular borehole remain in contact with the wall for the vast majority of their length (see, e.g., Bedrossian et al., 1993). Moreover the present study has the advantage over traditional finite-element approaches that by treating arclength along the rod as time, powerful techniques from dyanamical systems theory become available. A more realistic treatment of a rod that is free to lift off from the interior of the cylinder will form the subject of future work.

Explosive bifurcation in the integrable case: We have seen that the integrable isotropic case exhibits a *heteroclinic explosion.* This is a bifurcation, new to elastic stability theory, that arises in long (strictly infinite) structures. The localised post-buckling solution suddenly explodes in size at a heteroclinic connection. This is a global bifurcation that lies outside the scope of conventional linear stability theory.

To examine the event in more detail, Fig. 13 shows sketches of the phase portrait (θ, θ') of the equivalent oscillator at different values of the *dead* loading parameter, m, superimposed on the elastic response curves of m versus the deflection parameter, θ_0 (the central Euler angle of the constrained and twisted rod). For all m in the sketch, the trivial fundamental path with $\theta_0 = 0$ is a *stable* state of the elastic system which corresponds to an *unstable* saddle point of the oscillator. However, it is assumed that at higher m the fundamental path loses its elastic stability at a critical point at m_c (in some examples, as in the present twisted rod, m_c is infinite). From this point, there are two unstable falling post-buckling paths. The first is a path of periodic solutions (the helical solution of the rod), corresponding to a centre of the Hamiltonian oscillator. The second is a path of localised solutions corresponding to orbits homoclinic to the trivial saddle solution. As m is decreased, the periodic path of the isotropic rod exhibits two folds (LP) bounding a region of stable elastic behaviour. This corresponds to a softening–hardening–softening post-buckling response.

Of particular interest is the collision between these two paths at H, corresponding to a heteroclinic connection between the two saddles of the oscillator. As m is decreased towards m_h, the homoclinic orbit spends longer and longer in its slow passage close to the periodic saddle. Correspondingly, the deformation of the long structure has a spreading nearly-periodic regime between its trivial asymptotes at plus and minus infinity.

Corresponding to this sketch, the actual solutions of the constrained isotropic rod are shown in Fig. 14 using the same axes.

Pinching and spreading of the localisation: A particularly interesting feature of the response that we have just described is the contrast between what we could call the *pinching of the envelope* and the *spreading of the saturation*, illustrated in Fig. 15. Here we have assumed that we have a finite buckling load, m_c. As m is decreased from m_c, the envelope of the buckling mode is pinched in a manner that is familiar from perturbation analysis. In contrast, as m is decreased further towards m_h, the central region saturates onto a periodic (helical) form, the extent of which increases to infinity as m_h is approached.

Heteroclinic tangles in the non-integrable case: As is well-known in dynamical systems theory, the perturbation of an integrable system into a non-integrable system generically changes a simple heteroclinic

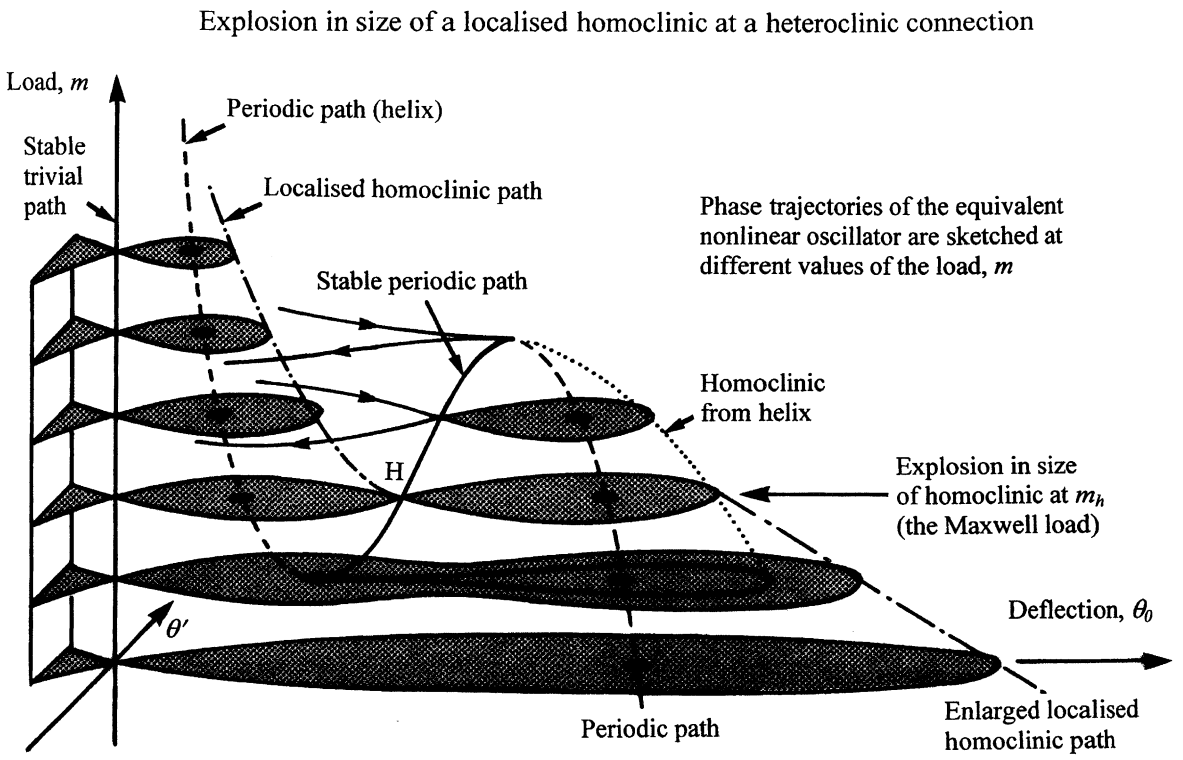

Fig. 13. Sketches of the phase portrait (θ, θ') of the equivalent oscillator at different values of the load, m, superimposed on the elastic response curves of m versus the deflection parameter, θ_0, illustrating the explosion in size of a localised homoclinic orbit at a heteroclinic connection.

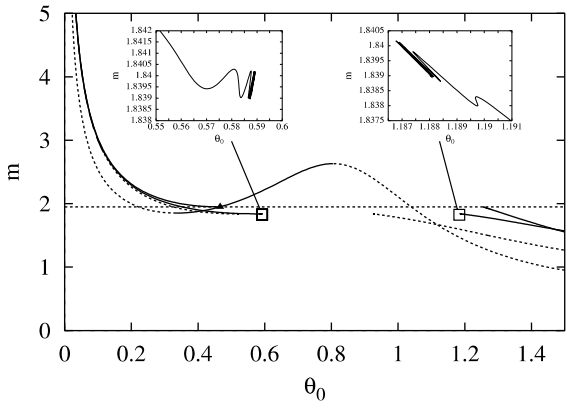

Fig. 14. Load–deflection diagram showing the explosive bifurcation in both the isotropic and anisotropic rod. Here $\theta_0 = \theta(0)$. The curve going through two LP is for helical solutions of the isotropic rod (the corresponding curve for the anisotropic rod is similar but not drawn). The other curves are for localised solutions and are the same as those in Fig. 4 but in a different representation. For the isotropic rod these curves reach to the critical load m_h indicated by the horizontal dotted line. The black triangle signifies the collision with the curve of helical solutions. For the anisotropic rod the curves end in oscillations. Solid curves (with enlargements) are for R_1^0-symmetric, dashed curves for $R_1^{\pi/2}$-symmetric anisotropic solutions ($\nu = 1/3$, $\tilde{r} = 0.8$).

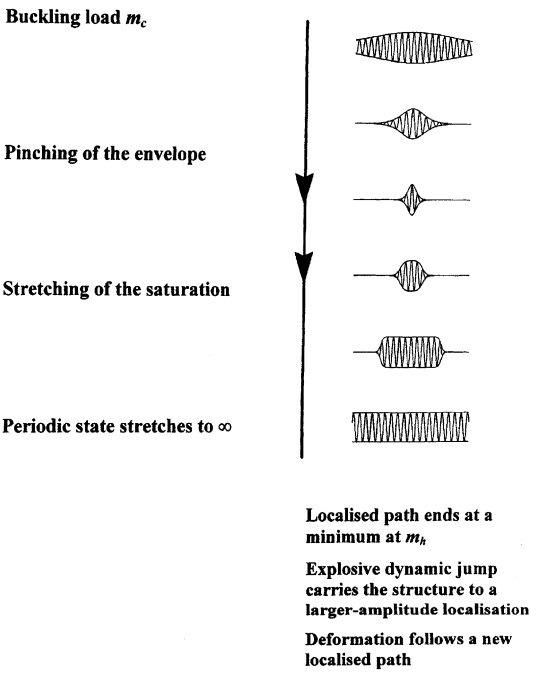

Fig. 15. 'Pinch and stretch localisation': the sequence of pinch and stretch as a structure follows the localised post-buckling path under reducing load from a critical buckling load m_c to a heteroclinic connection and explosion at m_h.

connection into a heteroclinic tangle. The latter manifests itself here as the rising snaking line of Figs. 4 and 5, similar to diagrams produced by Hunt et al. (1999) for the compressed cylindrical shell. However, on a plot of m versus θ_0 the tangles appear quite localised, as shown in Fig. 14 for the constrained anisotropic rod. The reason for this snaking is the interaction between the period of the helix and the period of the internal twisting. The two sections of rod currently being wound into a helical shape at the ends of the spreading saturated region will experience different orientations relative to the cylindrical surface as the process continues. Thinking of the anisotropic cross-section as being rectangular, there will be a period of *easy winding* when the rectangle has its long side oriented to lie in the cylindrical surface followed by a period of *hard winding* when the rectangle has its short side oriented to lie in the cylindrical surface. Apart from the heteroclinic tangle, anisotropy of the rod's cross-section also introduces multi-loop post-buckling solutions of which some examples have been presented in Section 3.

We finally mention that a novelty of the present system compared with the examples in Hunt et al. (2000) is that there is an integrable limit ($\rho = 0$), in which explicit results can be obtained. From this integrable limit the snaking towers in the load–deflection diagram emerge linearly (see Fig. 12). For other examples in Hunt et al. (2000), for instance the axially loaded cylindrical shell, the snaking was seen to emerge as an *exponentially flat* phenomenon out of a degenerate (super- to subcritical transition) linear buckling load of the trivial solution.

References

Antman, S.S., 1995. Nonlinear Problems of Elasticity. Springer, Berlin, New York.

Bai, F., Lord, G.J., Spence, A., 1996. Numerical computations of connecting orbits in discrete and continuous dynamical systems. Int. J. Bifurcation Chaos 6, 1281–1293.

Bedrossian, A.N., Abbassian, F., Dunayevsky, V.A., Hope, S.A. 1993. Analysis of post-buckling behaviour of drillstrings. 8th UK ABAQUS User Group Conference, 15 September 1993, Leicester University.

Doedel, E.J., Champneys, A.R., Fairgrieve, T.R., Kuznetsov Yu.A., Sandstede, B., Wang, X.J. 1997. AUTO97: Continuation and bifurcation software for ordinary differential equations. (Available by anonymous ftp from ftp.cs.concordia.ca/pub/doedel/auto).

Hairer, E., Nørsett, S.P., Wanner, G., 1993. Solving Ordinary Differential Equations I: Nonstiff Problems, second ed. Series in Computational Mathematics, vol. 8, Springer, Berlin, New York.

Hairer, E., Nørsett, S.P., Wanner, G. 1996. Solving Ordinary Differential Equations II: Stiff and Differential–Algebraic Problems, second ed., Series in Computational Mathematics, vol. 14, Springer, Berlin, New York.

Huang, N.C., Pattillo, P.D., 2000. Helical buckling of a tube in an inclined wellbore. Int. J. Non-linear Mech. 35, 911–923.

Hunt, G.W., Lord, G.J., Champneys, A.R., 1999. Homoclinic and heteroclinic orbits underlying the post-buckling of axially-compressed cylindrical shells. Comput. Meth. Appl. Mech. Eng. 170, 239–251.

Hunt, G.W., Peletier, M.A., Champneys, A.R., Woods, P.D., Wadee, M.A., Budd, C.J., Lord, G.J., 2000. Cellular buckling in long structures. Nonlinear Dyn. 21, 3–29.

Mielke, A., Holmes, P., 1988. Spatially complex equilibria of buckled rods. Arch. Rat. Mech. Anal. 101, 319–348.

Peletier, M.A. 2001. Sequential buckling; a variational analysis. Techincal Report: CWI, Amsterdam, MAS-R9920.

Seemann, W., 1996. Deformation of an elastic helix in contact with a rigid cylinder. Arch. Appl. Mech. 67, 117–139.

van der Heijden, G.H.M., Thompson, J.M.T., 1998. Lock-on to tape-like behaviour in the torsional buckling of anisotropic rods. Physica D 112, 201–224.

van der Heijden, G.H.M., Champneys, A.R., Thompson, J.M.T., 1999a. The spatial complexity of localised buckling in rods with non-circular cross-section. SIAM J. Appl. Math. 59, 198–221.

van der Heijden, G.H.M., Champneys, A.R., Thompson, J.M.T., 1999b. Spatially complex localisation in twisted elastic rods constrained to lie in the plane. J. Mech. Phys. Solids 47, 59–79.

van der Heijden, G.H.M., Thompson, J.M.T., 2000. Helical and localised buckling in twisted rods: a unified analysis of the symmetric case. Nonlinear Dyn. 21, 71–99.

van der Heijden, G.H.M., 2000. Bifurcation sequences in the interaction of resonances in a model deriving from nonlinear rotordynamics: the zipper. Dyn. Stab. Syst. 15, 159–183.

van der Heijden, G.H.M., 2001. The static deformation of a twisted elastic rod constrained to lie on a cylinder. Proc. R. Soc. London A 457, 695–715.